Combustion and Flame 277 (2025) 114175

Contents lists available at ScienceDirect

Combustion and Flame

journal homepage: www.sciencedirect.com/journal/combustion-and-flame

Active control of thermoacoustic instability in a lean-premixed hydrogen-enriched combustor via open-loop acoustic forcing

Yu Liao [a,b], Yongseok Choi [c], Peijin Liu [b], Kyu Tae Kim [c,*], Yu Guan [a,*]

[a] Department of Aeronautical and Aviation Engineering, The Hong Kong Polytechnic University, Kowloon, Hong Kong
[b] National Key Laboratory of Solid Rocket Propulsion, Northwestern Polytechnical University, Xi'an, 710072, China
[c] Department of Aerospace Engineering, Korea Advanced Institute of Science and Technology, Daejeon, 34141, Republic of Korea

ARTICLE INFO

Keywords:
Open-loop control
Thermoacoustic instability
Hydrogen-enriched combustion
Flame dynamics

ABSTRACT

Open-loop control is proven effective in mitigating self-excited oscillations in conventional hydrocarbon-fueled combustors, but its effectiveness in hydrogen-fueled combustors remains unknown. This study experimentally investigates the effectiveness of open-loop acoustic forcing in mitigating self-excited periodic thermoacoustic oscillations in a lean-premixed, hydrogen-enriched turbulent combustor. We conducted experiments across a range of hydrogen volume fractions (20% to 50%), varying both the frequencies and amplitudes of the acoustic forcing introduced via three loudspeakers positioned upstream of the combustor. For the first time, we have demonstrated the effectiveness of open-loop acoustic forcing in mitigating self-excited periodic thermoacoustic oscillations in a hydrogen-enriched combustor, with suppression effects becoming more pronounced as the hydrogen content increases. We achieve up to a 90% reduction in pressure amplitude with minimal energy input—less than 1% of the combustor's thermal power. At lower hydrogen fractions, the acoustic forcing fails to effectively decouple the flame dynamics from the acoustic field, resulting in significant oscillation amplification, with natural mode amplitudes increasing by over 2000%. A critical transition from global amplification to suppression occurs at a hydrogen volume fraction of 40%, where successful decoupling between the flame dynamics from the acoustic field is observed. These findings highlight the potential of open-loop control for mitigating thermoacoustic oscillations in hydrogen-enriched combustion systems, offering a promising approach to aid the decarbonization of gas turbines.

Novelty and significance statement

This study provides the first experimental evidence that open-loop acoustic forcing can effectively suppress thermoacoustic oscillations in hydrogen-enriched turbulent combustors. We show that increasing hydrogen volume fraction (20% to 50%) in the reactant mixtures enhances oscillation suppression, achieving up to a 90% reduction in pressure oscillation amplitude with minimal energy input (less than 1% of thermal power). A critical transition from oscillation amplification to suppression occurs at a hydrogen volume fraction of 40%, highlighting a threshold where decoupling between flame dynamics and the acoustic field becomes effective. These findings demonstrate the potential of open-loop control for stable operation in future hydrogen-enriched gas turbines.

1. Introduction

Hydrogen (H_2) stands out as a promising alternative to conventional hydrocarbon fuels, offering zero carbon emissions and high specific energy density, making it a key component in the transition to sustainable energy solutions within the aviation and energy sectors powered by gas turbines [1,2]. Leveraging this potential, the development of "green" H_2—produced through water electrolysis powered by renewable electricity sources such as solar and wind—marks a significant step toward a carbon-free society. However, adding H_2 into reactant mixtures significantly alters their combustion characteristics relative to conventional hydrocarbon fuels. This shift increases the likelihood of flashback due to H_2's high flame speed, facilitates autoignition because of its wider flammability limits, and leads to elevated NO_x emissions owing to H_2's higher adiabatic flame temperature [3]. Additionally, lean-premixed combustion is inherently prone to thermoacoustic instability, a phenomenon arising from strong coupling between oscillations in pressure and heat release rate (HRR) within the combustor [4,5].

* Corresponding authors.
E-mail addresses: kt_kim@kaist.ac.kr (K.T. Kim), yu.guan@polyu.edu.hk (Y. Guan).

https://doi.org/10.1016/j.combustflame.2025.114175
Received 19 November 2024; Received in revised form 4 April 2025; Accepted 5 April 2025
Available online 30 April 2025

Unfortunately, enriching reactant mixtures with H_2 further exacerbates thermoacoustic instability due to H_2's higher reactivity and burning rates [3]. These challenges pose limitations to the broader adoption of H_2 in gas turbines.

1.1. Thermoacoustic instabilities in H_2-fueled combustors

Previous studies have demonstrated that the addition of H_2 into reactant mixtures significantly alters flame dynamics and thermoacoustic stabilities. For example, Janus et al. [6] observed that a 25% volume fraction of H_2 shifted the unsteady region in the stability map of a premixed, swirl-stabilized CH_4/H_2 combustor toward lower airflow rates and equivalence ratios. This shift is attributed to the shorter chemical reaction time associated with H_2 addition. Similarly, Shanbhogue et al. [7] examined the transition process of swirl-stabilized premixed CH_4/H_2 flames under both acoustically coupled and decoupled conditions, with H_2 volume fractions reaching 50%. Their findings revealed that increasing the equivalence ratio caused the flame to exhibit four distinct shapes; under acoustically coupled conditions, H_2 addition lowered the critical equivalence ratio for the transition from steady combustion to self-excited oscillations. Similarly, Aguilar et al. [8] noted that increasing H_2 volume fraction in CH_4/H_2 mixture, while holding thermal power and equivalence ratio constant, led to significant changes in flame topology. Beyond a critical H_2 volume fraction, higher amplitude pressure oscillations were observed. Studies on premixed turbulent combustion systems fueled by pure H_2 have revealed distinct thermoacoustic behaviors. For example, Æsøy et al. [9] conducted experiments and modeled the flame transfer function of lean-premixed M flames, finding that at comparable thermal power levels, the cutoff frequency for pure H_2 flames was higher, while the time delay was shorter compared to CH_4/H_2 mixtures. The injector geometry also matters when burning H_2. For example, Lee and Kim [10] reported high-frequency transverse thermoacoustic modes (3.1 to 3.5 kHz), corresponding to the first tangential mode of the combustion chamber, in a lean-premixed pure H_2 combustor with a multislit injector configuration. By contrast, when burning pure H_2 in a combustor with a multinozzle injector configuration, only longitudinal thermoacoustic modes were observed [11]. Moreover, complex patterns of thermoacoustic mode interactions emerged in can-annular combustors with acoustic coupling via the annulus. For example, Moon et al. [12] identified a new modal interaction pattern—the local push-push mode—specific to the pure H_2 case, in contrast to previous findings in CH_4 combustion systems [13]. In a quick summary, adding H_2 to reactant mixtures significantly impacts combustion characteristics, including flame morphology and response, which in turn affect the properties (e.g., amplitude and frequency) and characteristics (e.g., onset conditions, nonlinear dynamics) of thermoacoustic instability in turbulent combustion systems. These changes are closely linked to the development of control strategies targeting thermoacoustic instabilities, suggesting that existing strategies originally designed for conventional hydrocarbon fuel combustors may require adaptation for H_2-enriched combustion systems.

1.2. Active control of thermoacoustic instabilities in turbulent combustors

Control strategies for suppressing thermoacoustic oscillations can be categorized into passive control and active control. A common passive control approach involves installing devices that enhance acoustic damping, such as acoustic liners [14,15], Helmholtz resonators [16], and porous cylinders [17]. More broadly, passive control includes any modifications to combustion facilities—such as injectors [18], swirler type [19], mixers [20], upstream ducts [21], annuli [22], and operating conditions [23]—that disrupt interactions among flow, flame, and acoustics to ultimately prevent the establishment of energy feedback loops. However, passive control strategies are often limited by a narrow effective frequency range and specific operating conditions, and they often require a comprehensive understanding of the system for optimal design [24]. In the transition to pure H_2 combustion, minimal modifications to existing combustion facilities would be more cost-effective, making passive control less favorable. In contrast, numerous active control strategies, offering greater operational flexibility across a broader range of conditions, have already been proven effective in suppressing thermoacoustic oscillations in conventional hydrocarbon-fueled gas turbines. Our study, therefore, advocates for active control, which uses fuel or acoustic modulation via specific actuators (e.g., loudspeakers or solenoid valves) to disrupt the energy feedback loop between pressure and HRR oscillations in combustors [25,26]. Active control strategies can be further divided into closed-loop and open-loop control approaches, depending on whether the control law will be adjusted based on real-time system response measured by sensors [27].

1.2.1. Closed-loop control

Closed-loop control in turbulent combustors typically includes two common types: feedback and self-adaptive control, both of which rely on one or more control feedback loops. Real-time data from the combustion chamber, such as pressure oscillations, serve as input to the control system. The controller processes these signals to generate an appropriate control response, which is then transmitted to actuators to make the necessary adjustments. This sequence completes the control feedback loop, targeting the suppression of thermoacoustic oscillations in turbulent combustors [27,28]. Feedback control has been applied to turbulent combustors since the 1990s. For example, Langhorne et al. [29] implemented feedback control in a 0.25 MW turbulent burner by introducing a time delay between the secondary injector's fuel supply and the pressure signal upstream of the combustion region, achieving over 80% reduction in low-frequency (0 to 400 Hz) acoustic energy. Siemens effectively applied active instability control to its Vx4.3A series heavy-duty gas turbines by equipping each combustion chamber with a direct-drive valve to independently modulate pilot fuel injection [30]. This approach successfully suppressed azimuthal thermoacoustic modes across various burner configurations and achieved a 60% reduction in NO_x emissions, with high operational reliability. Additionally, Murugappan et al. [31] used an extremum-seeking control algorithm in a 30 kW swirl-stabilized turbulent combustor, achieving up to 80% reduction in pressure and HRR oscillations. Paschereit et al. [32] also showed that upstream acoustic forcing can effectively mitigate thermoacoustic oscillations, yielding a 5 dB reduction in pressure oscillations amplitude and a 24% decrease in NO_x emissions. Further, Morgans and Stow [33] developed two closed-loop control strategies for annular combustors using a low-order thermoacoustic network model, including distributed controllers to manage coupled thermoacoustic modes and optimized transfer functions to reduce the number of sensors needed. In contrast, adaptive control offers a distinct advantage over traditional fixed-parameter feedback control, which depends on predefined control laws, by dynamically adjusting to optimize performance across various operating conditions [24]. Unlike fixed-parameter approaches, adaptive control eliminates the need for prior knowledge of thermoacoustic modes and combustion characteristics [27]. This method has been successfully applied in turbulent combustion systems, allowing real-time optimization of phase shifts to reduce thermoacoustic oscillations [34–36].

1.2.2. Open-loop control

Open-loop control, while less flexible in operation compared to closed-loop control, has been demonstrated effectiveness in mitigating thermoacoustic oscillations with lower hardware requirements and simpler control laws. The primary open-loop approach involves modulating either the fuel flow alone or the reactant mixtures at a non-resonant frequency, a method later characterized as asynchronous quenching (AQ) from the perspective of dynamical systems theory [37]. For example, Richards et al. [38] employed periodic modulation of the equivalence ratio in a full-scale gas turbine by individually adjusting each fuel injector to ensure at least half of the injectors operated under stable conditions, thereby achieving a reduction of oscillations amplitude by more than 30%. Yi and Gutmark [39] experimentally studied the application of open-loop acoustic forcing in a swirl-stabilized combustor. This approach achieved a suppression of pressure oscillations by up to 36.5 dB through the injection of sinusoidal air forcing into the swirling shear layer, with only a minimal increase of less than 1% in combustion air usage. Bellows et al. [40] applied acoustic forcing in a 10 kW swirl-stabilized burner, achieving frequency locking and reducing natural mode amplitude by over 90%. However, when self-excited amplitudes were too high, quenching was not achieved, and the instability shifted to a higher frequency. Ćosić et al. [41] extended this approach in a 100 kW swirl-stabilized combustor, demonstrating that open-loop acoustic forcing and premixed fuel flow modulation could reduce pressure oscillations by over 50% at non-resonant frequencies. Balusamy et al. [42] reported rich forced synchronization dynamics, including quasiperiodicity and the route to synchronization via a torus-death bifurcation. Lückoff and Oberleithner [43] explored open-loop acoustic forcing in a partially premixed swirl-stabilized combustor, finding that the amplitude of thermoacoustic oscillations could be reduced by over 80% with minimal power costs (under 1% of total momentum) due to enhanced mixing from precessing vortex core-induced equivalence ratio stabilization. Another unique approach by Mahesh et al. [44] utilized increased swirler rotation rates in a lean-premixed turbulent combustor, suppressing the first acoustic mode amplitude by around 25 dB by intensifying vortex breakdown and broadening the flame base angle. We also noted emerging open-loop control strategies using plasma [45,46], which have shown promising effectiveness in mitigating thermoacoustic oscillations. In addition to the highlighted effectiveness of open-loop control, the system responses examined in these studies provide crucial insights for developing more advanced closed-loop control algorithms. Furthermore, the ease of deploying open-loop control, owing to its lack of sensor requirements and immunity to signal transmission delays caused by hardware or harsh environmental conditions, makes it particularly suitable for practical applications. Therefore, we focus on investigating open-loop control in this study.

1.3. Aim of this study

H_2 addition in the reactant mixture significantly alters flame dynamics and the thermoacoustic stability of the combustor, as discussed in Section 1.1. While open-loop control has been proven effective in suppressing thermoacoustic oscillations in conventional hydrocarbon-fueled combustors, its potential in H_2-fueled combustors remains untested. Therefore, this study aims to experimentally investigate the effectiveness of open-loop acoustic forcing in mitigating thermoacoustic oscillations in a H_2-enriched turbulent combustor powered by a swirl-stabilized lean-premixed flame. Additionally, we will propose targeted improvements to enhance the adaptability of the open-loop control strategies for the current decarbonized combustor. Specifically, we focus on addressing the following key questions:

(1) Previous studies have demonstrated that open-loop acoustic forcing effectively weakens thermoacoustic oscillations in conventional hydrocarbon-fueled combustors at the off-resonant frequency and with sufficient forcing amplitudes. Is this control strategy still effective in mitigating thermoacoustic oscillations in a H_2-enriched turbulent combustor? What common characteristics does this H_2-enriched combustor share with previous conventional hydrocarbon-fueled combustors in terms of weakening thermoacoustic oscillations?
(2) If open-loop acoustic forcing is effective in suppressing thermoacoustic instabilities, how does its performance vary with different H_2 volume fractions in the fuel mixture? What are the optimal control strategies for open-loop acoustic forcing? What are the underlying physical mechanisms driving this control strategy?

To address these questions, we systematically test a wide range of H_2 volume fractions (from 0.2, the onset point of thermoacoustic instability, to 0.5, the upper limit beyond which flashback occurs), along with varying acoustic forcing frequencies and amplitudes, in a H_2-enriched turbulent combustion system (Section 2). We analyze the acoustic pressure and HRR signals, and flame images measured during the control process (Section 3). Finally, we conclude our study by discussing the limitations and practical implications of our findings (Section 4).

2. Experimental and analysis methods

2.1. Experimental setup and its diagnostics

The H_2-enriched turbulent combustion system and its diagnostic setup, shown in Fig. 1a, are identical to those previously used to investigate the acoustic communication and coupling-induced dynamics in can-annular combustors [47,48]. Air and fuel (H_2 and CH_4), metered respectively by two models of thermal mass flow meters (Sierra Instruments FlatTrak 780S, and Teledyne Instruments HFM-D-301), are fully mixed and sent into the setup through a choked plate located upstream, which serves to minimize disturbances from the inlet flow and establish a well-defined acoustic boundary condition. The measurement ranges for these flow meters are 6.8 kg/min for air, 0.36 kg/min for CH_4, and 0.058 kg/min for H_2. Their accuracy is $\pm$0.5% for air and $\pm$0.6% for fuel at full scale. When conducting open-loop acoustic forcing experiments, the acoustic forcing section, comprising three identical loudspeakers (Morel EW428) simultaneously driven by an amplified sinusoidal signal generated by a waveform generator (RIGOL DG4162) and a power amplifier (InterM R500Plus), acoustically forces the reactant mixture upstream of the flame. The maximum total output power of this acoustic forcing section is approximately 300 W. The reactant mixture is ignited at the dump plane of the combustor and stabilized by the upstream swirler (swirl number $S = 0.48$) and a central bluff body. The entire combustor consists of two parts: (a) an optically accessible fused quartz tube with an inner diameter of 109 mm and a length of 314 mm, cooled by an impinging forced convection air jet supplied via the concentric manifold to avoid being overheated by the high-temperature flame ($\sim$ 2000 K); and (b) a stainless steel tube, whose upstream end is cooled by a high-velocity air jet supplied via the outer concentric pipe at the upstream end. The downstream end of the stainless steel tube is exposed to ambient air and cooled by a combined forced and natural convection. The combustor length, L_c, is adjustable via a water-cooled movable piston at the end of the combustor. Both the piston and combustion products are cooled by the high-pressure quench water injected downstream (blue arrow in Fig. 1a) through fine spray nozzles at the rear surface of the piston head.

To quantify the intensity of acoustic perturbations introduced into the reactant mixture by the acoustic forcing section, a hot-wire anemometer (TSI 1210-10, TSI 1750) is positioned between the acoustic forcing section and the swirler. The intensity of acoustic perturbations, ϵ_f (i.e., forcing amplitude in the following content), is defined as the ratio of the velocity perturbation amplitude, u', over the bulk velocity, $\bar{u}$, i.e., $\epsilon_f \equiv u'/\bar{u}$. To measure the pressure oscillations in the combustor, p', a high-frequency response, water-cooled dynamic pressure transducer (PCB 112A22, sensitivity 14.5 mV/kPa, uncertainty $\pm$1%) is installed at the dump plane. The p' signal is sent to a signal conditioner (PCB 482C15) before being recorded by the data acquisition (DAQ) system. Meanwhile, to measure the global OH^* chemiluminescence intensity of the flame, which serves as an indicator of the flame's global HRR, q', a photomultiplier tube (PMT, Hamamatsu H7732-10) equipped with a band-pass interference filter (309 $\pm$ 5 nm) is placed near the combustor inlet. The estimated uncertainty in the chemiluminescence intensity measurement is approximately 1.0%, primarily due to variations in control voltage and the alignment of optical components. To study flame dynamics, a high-speed imaging system

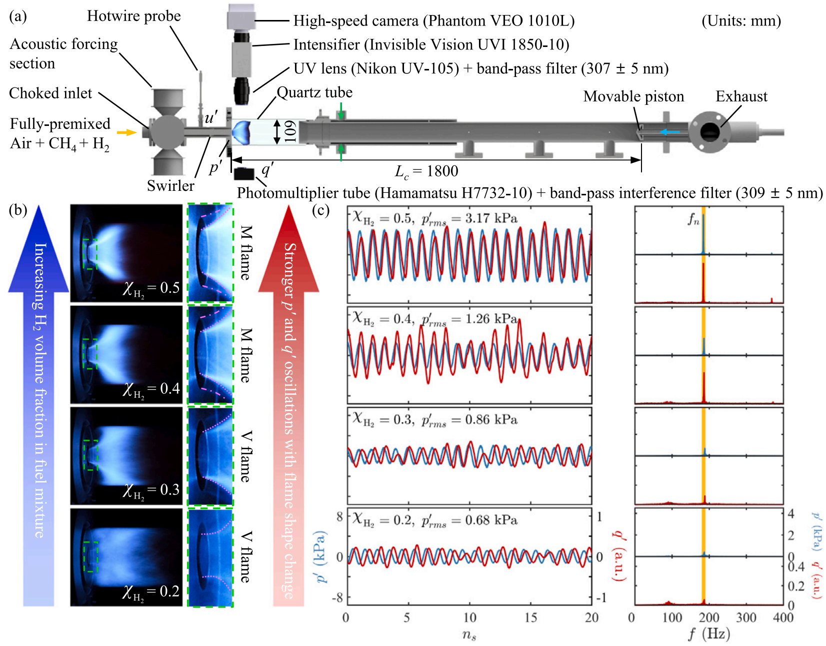

Fig. 1. (a) Rendered model of the H_2-enriched turbulent combustion system and its diagnostic setup (top view). A cross-sectional view of the model illustrates its internal structure, extending from the downstream of the acoustic forcing section to the upstream of the exhaust tube. The combustor length, L_c, can be adjusted using a movable piston, but is fixed at L_c = 1800 mm for this study. The orange arrow indicates the direction of the reactant mixture, while the green and blue arrows denote the cooling air and water flow channels, respectively. (b) Instantaneous flame images (left column) and magnified views of the flame root regions (right column), highlighted by the green dashed lines in the left column. In the right column of (b), the inner and outer flame boundaries are delineated by dotted and dash-dotted magenta lines, respectively, with the corresponding flame shape (V flame or M flame) labeled on the right. (c) Time series of pressure (p', blue) and HRR (q', red) oscillations as a function of the number of cycles of the self-excited mode, n_s (left column), and their FFT spectra (right column) for four self-excited cases of different H_2 volume fractions (0.2 to 0.5, from bottom to top row) in the H_2/CH_4 mixture, χ_{H_2}, defined as $V_{H_2}/(V_{CH_4}+V_{H_2})$. (For interpretation of the references to color in this figure legend, the reader is referred to the web version of this article.)

is positioned opposite the PMT on another side of the quartz tube. This imaging system consists of a high-speed camera (Phantom VEO 1010L), a UV camera intensifier (Invisible Vision UVI 1850-10), a UV lens (Nikon UV-105), and an OH* band-pass filter (Andover 307FS10-50 with a range of 307 ± 5 nm), which is capable of recording flame dynamics with a field of view of 720 × 720 pixels in a spatial resolution of about 0.1765 mm/pixel and a temporal resolution of 1/6000 s (frame rate of 6000 Hz). The total sampling time for each test is 8 s. Pressure, velocity, and OH* chemiluminescence signals are simultaneously digitized using a 16-bit high-speed DAQ system (TEAC LX-110) with a sampling frequency of 12 kHz and a total sampling time of 8 s. An external trigger signal is employed to synchronize the DAQ system with the high-speed imaging system.

2.2. Operating conditions

We focus on H_2 enrichment in the reactant mixture, with the H_2 volume fraction χ_{H_2}, defined as $V_{H_2}/(V_{CH_4}+V_{H_2})$, ranging from 0.2, below which thermoacoustic instability does not occur, to 0.5, beyond which the flashback occurs, with increments of 0.1. For all cases, we fix L_c to 1800 mm, and maintain a constant equivalence ratio of $\phi = 0.8$, with an overall uncertainty of 1.5%. We maintain the overall thermal power at P_{th} = 35 kW. The corresponding bulk velocity $\bar{u}$ is slightly adjusted for different χ_{H_2} values (from $\bar{u}$ = 21.1 m/s at χ_{H_2} = 0.2 to $\bar{u}$ = 21.2 m/s at χ_{H_2} = 0.5) to compensate for the change in reactant mixture volume caused by H_2 enrichment, resulting in a Reynolds number of $Re \approx 22000$. The adiabatic flame temperature is estimated to be around 2000 K, calculated using Cantera [49] based on the GRI 3.0 mechanisms [50]. Under these conditions, the natural frequency of self-excited oscillations f_n across different χ_{H_2} is found to be approximately 185 Hz, corresponding to the first-order longitudinal mode of the combustor. When conducting open-loop acoustic forcing experiments, it is challenging to precisely control the output power to force the system with completely identical ϵ_f across different frequencies because (i) the loudspeaker responds differently at different frequencies given the same input voltage, and (ii) the physicochemical properties (e.g., density) of the reactant mixture varies for different χ_{H_2}, which slightly affects the acoustic forcing amplitude. Therefore, we first use the output voltage of the signal generator (peak-to-peak value, A_f = 0 to 4 V) as the control parameter, with increments of ΔA_f = 0.1 V. We then calibrate the acoustic perturbation measured by the hot-wire anemometer into ϵ_f, which gives a maximum value of ϵ_f ranging from 20% to 70%. We choose forcing frequencies, f_f, in a normalized frequency ratio range of $f_r = f_f/f_n$ = 0.75 to 1.25, with increments of Δf_r = 0.05. Such a parameter space is broad enough, in which both the entire open-loop control process and rich synchronization dynamics [51,52] can be observed.

2.3. Analysis methodologies

To investigate nonlinear dynamics of the forced self-excited thermoacoustic oscillator under different forcing conditions, we use phase space reconstruction, a nonlinear time series analysis tool widely used to visualize attractors in phase space before [53]. This method is grounded in Takens' time-delay embedding theorem [54], which unfolds the dynamical properties of a multi-dimensional attractor using a one-dimensional scalar time series. In this study, we reconstruct the system's phase space using time series data of p' and q'. Using time series of p' as an example, its d-dimensional time-delay embedded vector is defined as $\boldsymbol{P}'_i(d) = [p'_i, p'_{i-\tau}, p'_{i-2\tau}, \ldots, p'_{i-(d-1)\tau}]$, where $i = (d-1)\tau+1, \ldots, N$, represents the ith reconstructed state vector [55]. We determine the optimal time delay τ and embedding dimension d using the first local minimum of the average mutual information [56] and Cao's method [57], respectively. This process is similarly applied to the time series of q'. Additionally, we use the Hilbert transform to compute the instantaneous phases of time series data of p' and q' [52], and then determine the instantaneous phase difference between them (i.e., $\Delta\psi_{\tilde{p}'-\tilde{q}'}$).

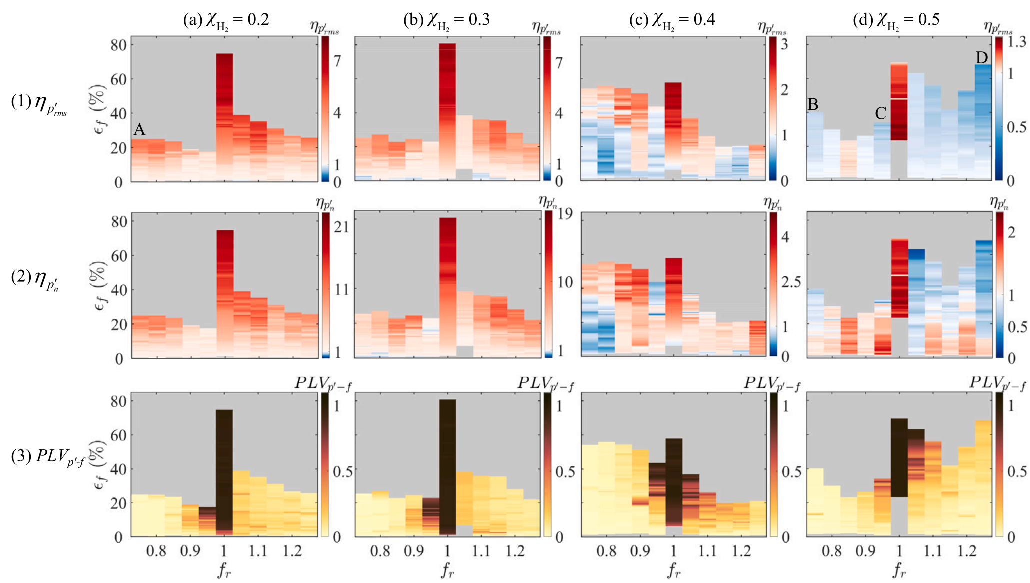

Fig. 2. Maps of the overall system response to open-loop acoustic forcing within a parameter space defined by the forcing amplitude, ϵ_f, and normalized forcing frequency, f_r for four different H_2 volume fractions (from left to right), $\chi_{H_2} = 0.2$ to 0.5. Three rows show (1) variation in global oscillation amplitude, $\eta_{p'_{rms}}$; (2) variation in the f_n mode amplitude, $\eta_{p'_n}$; and (3) phase locking value between p' and the open-loop acoustic forcing signals, $PLV_{p'-f}$. (For interpretation of the references to color in this figure legend, the reader is referred to the web version of this article.)

3. Results and discussion

3.1. Unforced thermoacoustic oscillations at different χ_{H_2}

We first examine thermoacoustic oscillations at varying χ_{H_2} levels without open-loop acoustic forcing. As shown in Fig. 1b, c, we present instantaneous flame images, time series of pressure (p') and HRR (q') oscillations as a function of the cycle count of the self-excited mode, n_s, along with their FFT spectra for self-excited cases across four different χ_{H_2} values (0.2 to 0.5), shown from bottom to top. As χ_{H_2} increases from 0.2 to 0.5, the flame transitions from a V flame to a more compact M flame, characterized by a reduced flame height and diminished flame-wall interaction (Fig. 1b, left column), resulting in a shorter and more compact flame. The flame root is further magnified in the right column of Fig. 1b to visualize the differences between the V flame and M flame: the V flame appears at lower $\chi_{H_2} = 0.2/0.3$, characterized by a single inner flame boundary (dotted magenta line) attached to the central bluff body. In contrast, the M flame appears at higher $\chi_{H_2} = 0.4/0.5$, characterized by the coexistence of the inner flame boundary (dotted magenta line) and an outer flame boundary (dot-dashed magenta line), indicating that the flame is anchored at both the central bluff body and the nozzle rim. Meanwhile, both p' and q' oscillations intensify with increasing χ_{H_2}. Time series of p' and q' evolve from low-amplitude aperiodic oscillations to high-amplitude periodic oscillations, as seen in Fig. 1c, left column. This evolution in the time domain is also evident in the frequency domain, where the natural frequency peak, whose location is highlighted by the orange shading, evolves from a subtle bump to a prominent, discrete peak in FFT spectra (Fig. 1c, right column). Based on all observations of the unforced thermoacoustic behavior of this system, we conclude that (1) thermoacoustic instability is triggered and intensified as χ_{H_2} increases; (2) the transformation of flame's shape from V-shape to M-shape is attributed to increased flame propagation speed and enhanced resistance to strain rates with increased χ_{H_2} [58,59], which likely will affect the flame response significantly [9]. These factors are expected to play a critical role in influencing the effectiveness of control strategies, which we will explore in the following section.

3.2. Overall system response to open-loop acoustic forcing

We examine the overall system response to open-loop acoustic forcing within a parameter space defined by the forcing amplitude, ϵ_f, normalized forcing frequency, f_r, and H_2 volume fraction, χ_{H_2}. This response, in terms of pressure oscillations, is evaluated using three key measures: variation in global oscillations amplitude, $\eta_{p'_{rms}}$; variation in the self-excited frequency f_n mode amplitude, $\eta_{p'_n}$; and phase locking value (PLV), $PLV_{p'-f}$, as illustrated in Fig. 2. The same measures are applied to HRR oscillations, as shown in Fig. 3. Three key measures are defined as follows:

- Variation in global oscillations amplitude:

$$\eta_{p'_{rms}} = \sigma(p'_{WF})/\sigma(p'_{WOF}) \tag{1}$$

where $\sigma(p'_{WF})$ and $\sigma(p'_{WOF})$ denote the root mean square of global pressure oscillations amplitude when the system is forced and unforced, respectively. $\eta_{p'_{rms}} > 1$ and $\eta_{p'_{rms}} < 1$ represent the amplification and suppression of global thermoacoustic oscillations, respectively.

- Variation in the f_n mode amplitude:

$$\eta_{p'_n} = A_{p'_{n,WF}}/A_{p'_{n,WOF}} \tag{2}$$

where $A_{p'_n}$ denotes the FFT amplitude at f_n. Subscripts WOF and WF correspond to the case without and with open-loop acoustic forcing, respectively. $\eta_{p'_n} > 1$ and $\eta_{p'_n} < 1$ represent the amplification and suppression of the f_n mode amplitude, respectively.

- Phase locking value (PLV) [60]:

$$PLV_{p'-f} = \left| \frac{1}{N} \sum_{n=1}^{N} e^{i\Delta\psi_{p'-f}} \right| \tag{3}$$

where $\Delta\psi_{p'-f}$ denotes the phase difference between p' and open-loop acoustic forcing signals, and N denotes the number of data points. The PLV quantifies the degree of synchronization [61] between p' and the open-loop acoustic forcing signals: $PLV_{p'-f} = 0$ signifies the f_n mode is the only dominant mode in p', $PLV_{p'-f} = 1$ signifies p' signal completely locks into the open-loop acoustic forcing signal, thus the f_f mode is the only dominant mode in

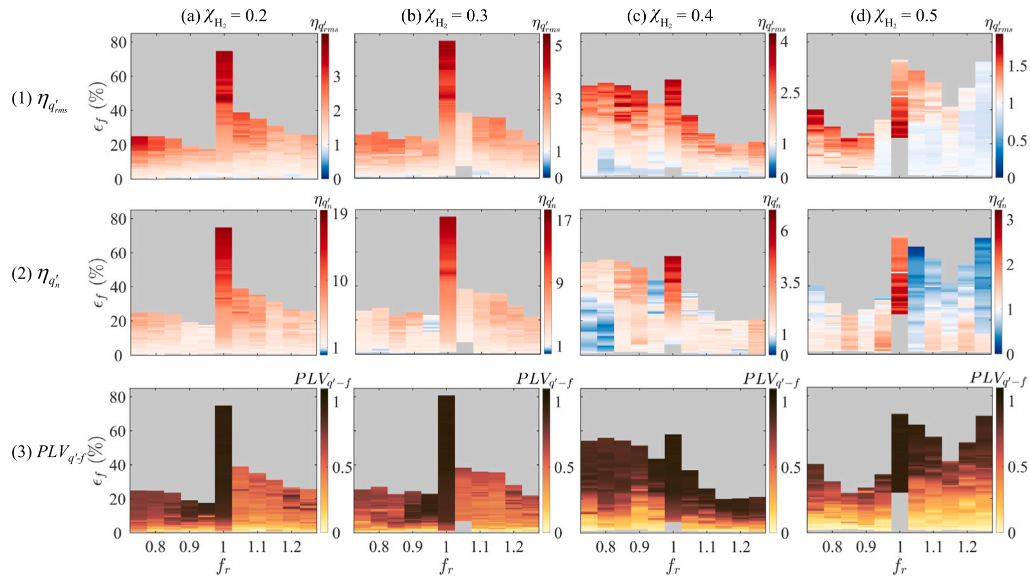

Fig. 3. The same as for Fig. 2 but for the case of q', with three rows showing (1) $\eta_{q'_{rms}}$, (2) $\eta_{q'_n}$, and (3) $PLV_{q'-f}$. (For interpretation of the references to color in this figure legend, the reader is referred to the web version of this article.)

p', and $PLV_{p'-f} \in (0, 1)$ indicates an asynchronous two-frequency quasiperiodic state where the f_n and f_f modes coexist.

The definitions of the three measures described above can also be applied to q', resulting in the corresponding terms $\eta_{q'_{rms}}$, $\eta_{q'_n}$, and $PLV_{q'-f}$ by substituting p' with q' in Eqs. (1)–(3). Rows (1) and (2) in Figs. 2 and 3 show how p' and q' are amplified (red, $\eta > 1$) or suppressed (blue, $\eta < 1$), with darker colors indicating stronger effects. As mentioned in Section 2.2, we control the output voltage from the signal generator (peak-to-peak value, $A_f = 0$ to 4 V), and then convert the acoustic perturbations measured using hot-wire anemometer to ϵ_f. Due to the inconsistent response of the loudspeaker to input voltage at different frequencies, data cannot be obtained in certain regions of the parameter space defined by ϵ_f and f_r, as indicated by the gray shading in Figs. 2 and 3. Nevertheless, we can still conduct a comprehensive analysis across different χ_{H_2} values, as we will demonstrate in the following sections.

We start by examining $\eta_{p'_{rms}}$ to acquire an overall view of how this H_2-enriched system responds to open-loop acoustic forcing, as shown in Fig. 2a1 to d1. When $\chi_{H_2} \leqslant 0.3$, the region of oscillation suppression is absent, implying the ineffectiveness of the open-loop acoustic forcing in weakening thermoacoustic oscillations. Two maps are predominantly reddish, suggesting that oscillation amplification dominates, both at resonant ($f_r = 1$, with maximum $\eta_{p'_{rms}}$ reaching over 740%) and off-resonant ($f_r = 1.10$, with maximum $\eta_{p'_{rms}} \approx 550\%$) forcing frequencies. This effect is likely due to two main factors: (i) the amplification of the self-excited mode (i.e., the f_n mode), and (ii) additional energy injected by open-loop acoustic forcing, thereby amplifying the forced mode (i.e., the f_f mode). When $\chi_{H_2} \geqslant 0.4$, several bluish regions, representing oscillation suppression, emerge in two maps, with more bluish regions emerging as χ_{H_2} increases. The most significant oscillation suppression is observed at $\chi_{H_2} = 0.5$. Specifically, the most pronounced global oscillation suppression occurs at $f_r = 1.25$ and $\epsilon_f \approx 70\%$, achieving a minimum $\eta_{p'_{rms}}$ of 37%.

Building on this observation, we proceed to examine $\eta_{p'_n}$ to determine if the observed oscillation suppression is likely due to a reduction in the f_n mode, as shown in Fig. 2a2 to d2. When $\chi_{H_2} \leqslant 0.3$, no reduction in the f_n mode is detected. Instead, the f_n mode tends to be amplified as ϵ_f increases, indicating that stronger open-loop acoustic forcing reinforces the f_n mode. For example, when the system is forced at the resonant frequency ($f_r = 1$), the maximum $\eta_{p'_n}$ exceeds 2000%. When $\chi_{H_2} \geqslant 0.4$, the f_n mode can be weakened at certain off-resonant frequencies. However, this suppression is not sustained; as ϵ_f continues to increase, the f_n mode eventually amplifies, especially at $\chi_{H_2} = 0.4$. This amplification is less intense at similar levels of ϵ_f when $\chi_{H_2} = 0.5$, which likely contributes to the more significant oscillation suppression and the broader regions of oscillation suppression seen in the map. Focusing on the f_n mode amplitude, the maximum oscillation occurs at $f_r = 1.05$, with a minimum of $\eta_{p'_n} = 10\%$ at $\epsilon_f \approx 60\%$.

Moving forward, we examine $PLV_{p'-f}$ to quantify the degree of synchronization between the thermoacoustic oscillator and open-loop acoustic forcing, as shown in Fig. 2a3 to d3. Across all maps at various χ_{H_2} levels, the regions away from $f_r = 1$ show consistently low $PLV_{p'-f}$ values, suggesting this thermoacoustic oscillator is hardly locked into the open-loop acoustic forcing. As a result, the f_n mode persists alongside the f_f mode across different f_r, ϵ_f, and χ_{H_2} conditions, even if the strength of the f_n mode varies. This finding suggests that the oscillation suppression observed in our study likely differs from previous works [40,42,62,63] where suppression of the natural mode was primarily responsible for global oscillation reduction.

Next, we focus on the forced response of the flame to gain a more direct understanding of the effects of open-loop acoustic forcing. The velocity perturbations introduced by the forcing directly impact the flame dynamics, which in turn influence the resulting pressure oscillations in the system. This approach allows us to see more clearly how forcing affects flame behavior and how this manifests in overall system response.

We start by examining $\eta_{q'_{rms}}$ and $\eta_{q'_n}$ to gain an overall understanding of the forced response of this H_2-enriched flame, shown in Fig. 3a1 to d2. When $\chi_{H_2} \leqslant 0.3$, $\eta_{q'_{rms}}$ behaves similarly to $\eta_{p'_{rms}}$, dominated by reddish regions, indicating that the overall gain of the f_n and f_f modes increases as ϵ_f rises. Likewise, $\eta_{q'_n}$ shows a moderate increase, particularly at off-resonant frequencies, suggesting that the f_n mode is amplified rather than dampened by the open-loop acoustic forcing. This results in both amplification of the f_n mode and the overall thermoacoustic oscillation discussed earlier. When $\chi_{H_2} \geqslant 0.4$, the behavior of $\eta_{q'_{rms}}$ and $\eta_{q'_n}$ diverges from that of $\eta_{p'_{rms}}$ and $\eta_{p'_n}$. First, the flame response becomes markedly stronger as ϵ_f increases, especially for $f_r \leqslant 0.9$, primarily due to a significant response at f_f. Additionally, amplification regions (reddish regions) appear on both sides of f_n, with particularly strong amplification at $f_r < 1$ when $\chi_{H_2} = 0.5$, indicating a more pronounced flame response to forcing at off-resonant

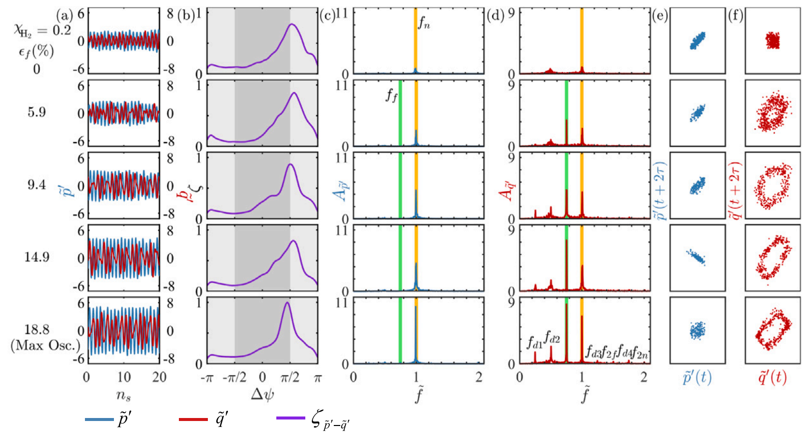

Fig. 4. Route to oscillation amplification when $\chi_{H_2} = 0.2$ and $f_r = 0.75$ (Case A): (a) Time series of normalized amplitudes, $\tilde{p}' \equiv p'/\sigma(p'_{WOF})$ and $\tilde{q}' \equiv q'/\sigma(q'_{WOF})$, as a function of cycle count, n_s, for the self-excited mode, (b) Histograms of wrapped phase differences for $\tilde{p}'$ and $\tilde{q}'$ ($\zeta_{\tilde{p}'-\tilde{q}'}$), Normalized FFT spectra of (c) $\tilde{p}'$ and (d) $\tilde{q}'$, and One-sided Poincaré maps of attractors reconstructed from (e) p' signal and (f) q' signal. In (b), the light and dark gray shading denote anti-phase and in-phase dynamics, respectively. In (c) and (d), the x-axis represents the normalized frequency, $\tilde{f} = f/f_n$. In (d), linear combinations and higher-order harmonics of f_n and f_f are denoted: $f_{d1} = |f_n - f_f|$, $f_{d2} = 2f_f - f_n$, $f_{d3} = 2f_n - f_f$, $f_{d4} = 4f_n - 3f_f$, $f_{2n} = 2f_n$, $f_{2f} = 2f_f$. (For interpretation of the references to color in this figure legend, the reader is referred to the web version of this article.)

frequencies lower than f_n. This also explains why less pronounced oscillation suppression is observed in this region.

We then examine $PLV_{q'-f}$ to investigate the degree of synchronization between the flame and open-loop acoustic forcing, as shown in Fig. 3a3 to d3. Unlike $PLV_{p'-f}$, these maps are significantly darker overall, indicating a higher degree of synchronization between the flame and forcing. When $\chi_{H_2} \leqslant 0.3$, $PLV_{q'-f}$ tends to be higher at $f_r < 1$, suggesting a stronger flame response to lower open-loop acoustic forcing frequencies. This response shifts as χ_{H_2} increases, with two notable effects: (i) synchronization becomes stronger at $f_r > 1$, indicating that the flame's response shifts toward higher frequencies with added H_2, and (ii) the overall map further darkens, reflecting an enhanced flame response to the open-loop acoustic forcing. This enhanced synchronization may explain why control becomes achievable with higher χ_{H_2}.

To summarize, our main findings in this section are as follows: (I) Open-loop acoustic forcing can effectively suppress self-excited thermoacoustic oscillations in this H_2-enriched turbulent combustor, but only when $\chi_{H_2} \geqslant 0.4$. The global thermoacoustic oscillations can be weakened to 37% of the unforced self-excited level (i.e., $\eta_{p'_{rms}} = 37\%$). This suppression is associated with a modified flame response to the forcing caused by the H_2 addition, as indicated by stronger synchronization between q' and the forcing signals; (II) The f_n mode persists across different ϵ_f levels and is not significantly weakened or locked onto f_f, which contrasts with prior studies where oscillation suppression often requires suppression of the f_n mode. In this study, even with significantly reduced global thermoacoustic amplitude, lock-in does not occur, highlighting a distinct behavior compared to previous studies in conventional hydrocarbon-fuel combustors; and (III) As χ_{H_2} increases, the flame responds more strongly to higher forcing frequencies, consistent with previous measurements of flame responses for H_2-enriched flames [8,58,64]. This shift in flame response also corresponds with more pronounced oscillation suppression and a larger region of oscillation suppression at higher forcing frequencies in our study.

3.3. Detailed control dynamics at fixed forcing frequencies

In this section, we will provide a detailed analysis of p', q', and the forcing signals across the time domain, frequency domain, and phase space, to investigate the control dynamics along routes where f_r remains fixed and only ϵ_f varies. For each path, we begin with the unforced base case and explore the system's response to open-loop acoustic forcing as ϵ_f increases. We select four representative cases (A–D, as marked in Fig. 2a1 to d1) to illustrate the forced response of the thermoacoustic oscillator across different χ_{H_2} values, detailing routes toward either oscillation amplification or suppression (see Figs. 4 to 7). Each figure presents a comprehensive analysis of both p' and q' signals, including (a) Time series of normalized amplitudes, $\tilde{p}' \equiv p'/\sigma(p'_{WOF})$ and $\tilde{q}' \equiv q'/\sigma(q'_{WOF})$, as a function of the cycle count of the f_n mode, (b) Histograms of wrapped phase differences for $\tilde{p}'$ and $\tilde{q}'$ ($\zeta_{\tilde{p}'-\tilde{q}'}$), Normalized FFT spectra of (c) $\tilde{p}'$ ($A_{\tilde{p}'}$) and (d) $\tilde{q}'$($A_{\tilde{q}'}$), and One-sided Poincaré maps of attractors reconstructed from (e) p' signal and (f) q' signal. ϵ_f increases from the top row to the bottom row.

3.3.1. Oscillation amplification

We first examine a representative case along the route to oscillation amplification (Case A, Fig. 4). We find that the system responds to open-loop acoustic forcing as ϵ_f increases:

- When $\epsilon_f = 0$, the system state is a limit cycle. This limit cycle is relatively weak, as indicated by slightly irregular time traces and short peaks in the FFT spectra of p' and q' signals (Fig. 4a,c,d), reflecting the initial onset of thermoacoustic instability. A large portion of the distribution of $\Delta\psi_{\tilde{p}'-\tilde{q}'}$ is in the anti-phase region (Fig. 4b), which is because the thermoacoustic instability just establishes when $\chi_{H_2} = 0.2$.
- When $\epsilon_f = 5.9\%$, the system remains in a limit cycle state, but the flame response becomes quasiperiodic. The additional acoustic energy introduced by the forcing at f_f is negligible, while the f_n mode is strengthened by the forcing, indicated by a stronger peak in the FFT spectrum of the p' signal (Fig. 4c). In the Poincaré map of the p' signal, the discrete point remains, confirming the system state is a limit cycle (Fig. 4e). In contrast, the flame responds positively to the forcing, as evidenced by an additional peak of similar height at f_f in the FFT spectrum of q' signal, alongside a higher f_n (Fig. 4d). In the Poincaré map of q' signal, this transition is manifested as the evolution from a discrete point to a ring-like structure (Fig. 4f), suggesting a transition in flame dynamics from a limit cycle to a torus via a Neimark-Sacker bifurcation [61]. Although both p' and q' signals amplify at f_n due to the forcing, no distinct peak emerges at f_f in the spectrum of the p' signal (Fig. 4c). As a result, the distribution of $\Delta\psi_{\tilde{p}'-\tilde{q}'}$ becomes broader and flatter, with the peak shifting further into the anti-phase region. This variation indicates a weakened coupling between the p' and q' signals, likely due to the increasing influence of the f_f component in the flame response (Fig. 4b).

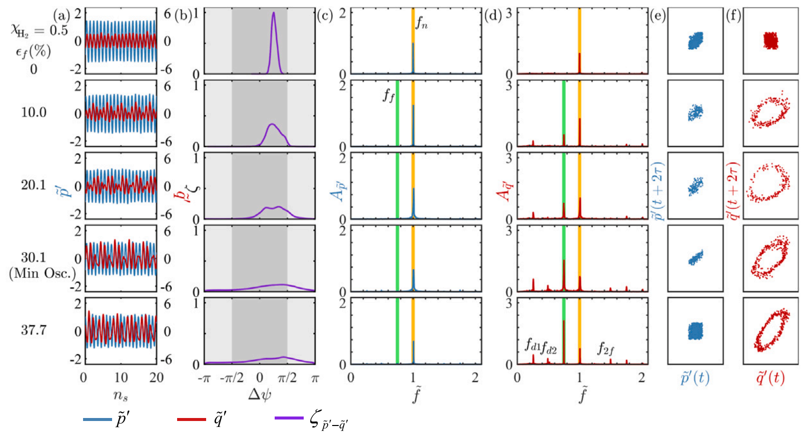

Fig. 5. The same as for Fig. 4 but along the route to oscillation suppression when $\chi_{H_2} = 0.5$ and $f_r = 0.75$ (Case B). (For interpretation of the references to color in this figure legend, the reader is referred to the web version of this article.)

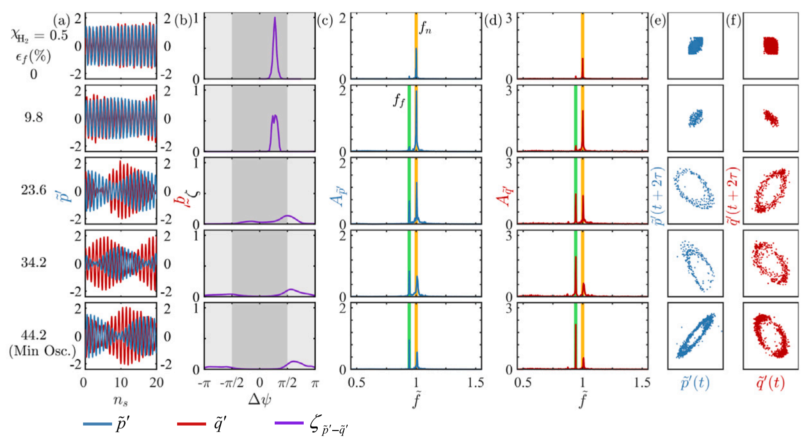

Fig. 6. The same as for Fig. 4 but along the route to oscillation suppression when $\chi_{H_2} = 0.5$ and $f_r = 0.95$ (Case C). (For interpretation of the references to color in this figure legend, the reader is referred to the web version of this article.)

- When $\epsilon_f \geqslant 9.4\%$ (up to the maximum achievable ϵ_f in both cases), the system remains in a limit cycle state, while the flame response consistently exhibits quasiperiodic behavior. The time trace of the p' signal exhibits a sinusoidal waveform, whereas the q' signal shows amplitude modulation, a characteristic feature of quasiperiodic behavior (Fig. 4a). The forcing fails to generate a noticeable peak at f_f in the FFT spectrum of the p' signal (Fig. 4c), indicating that the additional acoustic energy from the forcing has a minimal impact. This is likely because the forcing frequency f_f is not sufficiently close to the system's natural resonance frequency f_n to induce significant variations in pressure oscillations, allowing the f_n mode to remain dominant. The f_n mode is amplified to over 11 times stronger than the unforced state (Fig. 4c), leading to global oscillation amplification. In the FFT spectrum of q', peaks at f_f, f_n, and their linear combinations and higher-order harmonics become more pronounced, indicating that the flame is more responsive to velocity fluctuations at f_f from the forcing, despite f_f is not in the vicinity of f_n (Fig. 4d). The distribution of $\Delta\psi_{\tilde{p}'-\tilde{q}'}$ becomes more concentrated in the in-phase region and exhibits a narrower spread (Fig. 4b). This shift indicates a stronger coupling between the p' and q' signals, thereby enhancing oscillation amplification.

3.3.2. Oscillation suppression

We then turn our attention to three representative cases along the route to oscillation suppression: Case B (Fig. 5), Case C (Fig. 6), and Case D (Fig. 7). In each case, we observe that the system responds to open-loop acoustic forcing in a similar manner as ϵ_f increases.

- When $\epsilon_f = 0$, the system state is a strong limit cycle because the thermoacoustic instability is now fully established, characterized by smooth sinusoidal time traces and tall, discrete peaks for both p' and q' signals (Fig. 5a,c,d). $\Delta\psi_{\tilde{p}'-\tilde{q}'}$ becomes narrowly focused in the in-phase region, showing a sharp and narrow distribution (Fig. 5b), agreeing with the Rayleigh criterion. In addition, the presence of a single, solid blob in Poincaré maps of p' and q' signals, confirms the system's state and flame's dynamical behavior as a Period-1 limit cycle (Fig. 5e,f).
- When $\epsilon_f = 10.0\%$ and $f_r = 0.75$, the system maintains a limit cycle state for Case B, although the flame response starts to exhibit quasiperiodic behavior, similar to what was observed in Case A. However, as f_r increases, the additional acoustic energy introduced by the forcing at f_f becomes significant for Case C and D, especially when f_f is near f_n. For example, when $\epsilon_f = 23.6\%$ and $f_r = 0.95$, a noticeable peak at f_f appears in the FFT spectrum of the p' signal (Fig. 6c), causing the system to transition into a quasiperiodic state, as evidenced by the emergence of a ring-like structure in the Poincaré map (Fig. 6e). This dynamical transition from a Period-1 limit cycle to a two-frequency torus is also observed at $\epsilon_f = 15.6\%$ with $f_r = 1.25$ (Fig. 7e,f). A common feature across Cases B, C, and D is that the flame exhibits a positive response to the external forcing, leading to the emergence of a peak at f_f in the FFT spectrum of the q' signal (Figs. 5d,

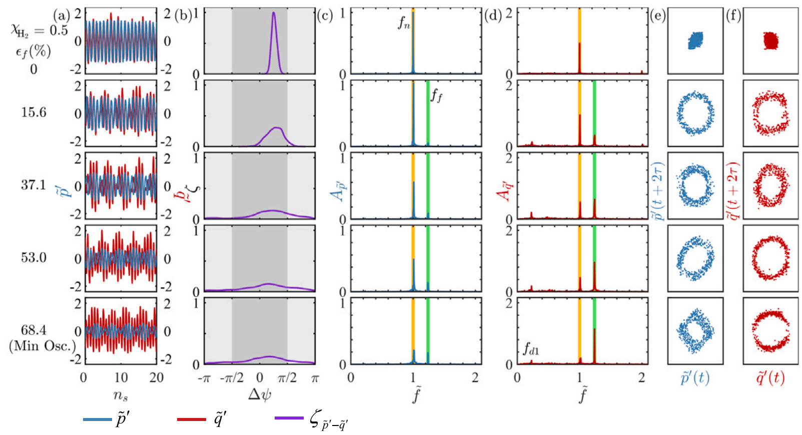

Fig. 7. The same as for Fig. 4 but along the route to oscillation suppression when $\chi_{H_2} = 0.5$ and $f_r = 1.25$ (Case D). (For interpretation of the references to color in this figure legend, the reader is referred to the web version of this article.)

6d, 7d). Consequently, ring-like structures consistently appear in the Poincaré maps for these cases (Figs. 5f, 6f, 7f), indicating the onset of quasiperiodic dynamics.

- When $\epsilon_f \geqslant 20.1\%$ for $\chi_{H_2} = 0.5$ (up to the maximum tested ϵ_f), the system in Case B always maintains a limit cycle state, while the flame response remains quasiperiodic. In this scenario, the time trace of the p' signal exhibits a smooth sinusoidal waveform, while the q' signal exhibits pronounced amplitude modulation, a characteristic feature of quasiperiodic behavior (Fig. 5a). The forcing fails to generate a noticeable peak at f_f in the FFT spectrum of the p' signal (Fig. 5c), indicating that the additional acoustic energy from the forcing has a minimal impact for this case. Meanwhile, the f_n mode is significantly weakened, with the normalized FFT amplitude of the p' signal ($A_{\tilde{p}'}$) dropping to 71.3% when $\epsilon_f = 30.1\%$ (Fig. 5c). Additionally, the distribution of $\Delta\psi_{\tilde{p}'-\tilde{q}'}$ flattens completely (Fig. 5b), indicating a severe disruption of the feedback loop between the flame and acoustics caused by the open-loop forcing and consequently leading to a suppression of pressure oscillations. A similar mechanism of oscillation suppression is observed in Cases C and D. In both instances, the f_n mode is notably diminished (Figs. 6c and 7c), and the distribution of $\Delta\psi_{\tilde{p}'-\tilde{q}'}$ also becomes fully flattened (Figs. 6b and Fig. 7b). This indicates a consistent pattern across the cases where the external forcing disrupts the coupling between the flame and acoustics, leading to a substantial reduction in the amplitude of the f_n mode. It is also noteworthy that no forced synchronization is observed in this study, even at the maximum oscillation suppression. Both the system and the flame response continue to exhibit quasiperiodic behavior (Figs. 5e,f, 6e,f and 7e,f), which contrasts with previous findings on laminar flames [37,65], where maximum suppression typically accompanies forced synchronization. One possible explanation for this difference is the presence of turbulence-induced noise, which tends to always amplify oscillations at f_n, making it nearly impossible to completely eliminate the f_n mode. This persistence of the f_n mode aligns with earlier observations in studies involving open-loop control of turbulent flames [40,42], where complete suppression of the f_n mode was also not achieved.

3.3.3. Flame dynamics: Oscillation amplification vs oscillation suppression

We now examine the flame dynamics of Case A (oscillation amplification) and Case D (oscillation suppression), considering both the time-averaged (Fig. 8) and phase-averaged (Figs. 9 and 10) OH* chemiluminescence intensity distributions. In the absence of external forcing, the flame topology exhibits distinct characteristics: a V-shaped flame in Case A (Fig. 8a, left) and an M-shaped flame in Case D (Fig. 8b, left), with corresponding flame heights of approximately 70 mm and 40 mm. As ϵ_f increases, the OH* intensity in Case A ($\chi_{H_2} = 0.2$) expands both upstream and downstream (Fig. 8a). This broadening of the flame boundary corresponds to an intensified HRR, as indicated by the pronounced peaks of $\tilde{q}'$ in Fig. 4d. The Abel-deconvoluted mean flame image for Case A further reveals a progressive transformation in HRR with increasing ϵ_f, where the initially thin, horn-shaped flame anchored at the central bluff body transitions into a thicker, inclined leaf-like structure, suggesting intensified axial flame oscillations.

In contrast, in Case D ($\chi_{H_2} = 0.5$), the flame remains more compact, exhibiting limited variation in both shape and intensity with increasing ϵ_f (Fig. 8b, left). This behavior is further corroborated by the Abel-deconvoluted mean flame image, which consistently retains a droplet-like shape anchored at both the central bluff body boundary and the nozzle rim, indicating a more concentrated HRR distribution. Additionally, the similarity in both flame pattern and intensity across different ϵ_f values suggests a saturation effect in the HRR, which is also evident in the comparable amplitude of $\tilde{q}'$ at different ϵ_f values, as shown in Fig. 7a.

To better understand the mechanism of oscillation amplification and suppression at different χ_{H_2}, we further examine the phase-resolved flame dynamics of these two representative cases at the maximum ϵ_f. Specifically, we compare the flame's mode shapes under both self-excited oscillations and acoustic forcing at f_n and f_f, respectively. For a more quantitative comparison, we align the phase reference by setting the initial phase to $p'_n = 0$ for both f_n and f_f cases (as indicated by the magenta dot labeled 1 in Fig. 11a). The time series of OH* chemiluminescence images is then processed using a band-pass filter corresponding to each frequency component to extract the respective OH* intensity distributions. These filtered images are subsequently phase-averaged over 20 cycles T ($T_n = 1/f_n$ and $T_f = 1/f_f$), with each cycle divided into 10 phase intervals. The resulting phase-averaged flame images are presented in Figs. 9 and 10, while the corresponding p' and q' variations are shown in Fig. 11a,b.

We first compare the flame's mode shapes of the two unforced, self-excited states: Case A (Fig. 9a, left) and Case D (Fig. 10a, left). As discussed in Section 3.1, the self-excited oscillation amplitude (p') in Case A is significantly smaller than in Case D due to stronger thermoacoustic oscillations in Case D, which result in a higher HRR. This is further reflected by the darker flame color in Case D. A comparison of the flame shapes at the same phase (t/T) reveals distinct OH* intensity distributions. In Case A, at $t/T = 0$, the minimum OH* intensity appears upstream, while the maximum OH* intensity appears downstream, with the low-intensity region gradually shifting downstream over time. In contrast, Case D shows the opposite pattern: the maximum OH* intensity is upstream, and the minimum OH* intensity is downstream, with the high-intensity region gradually propagating downstream. Since

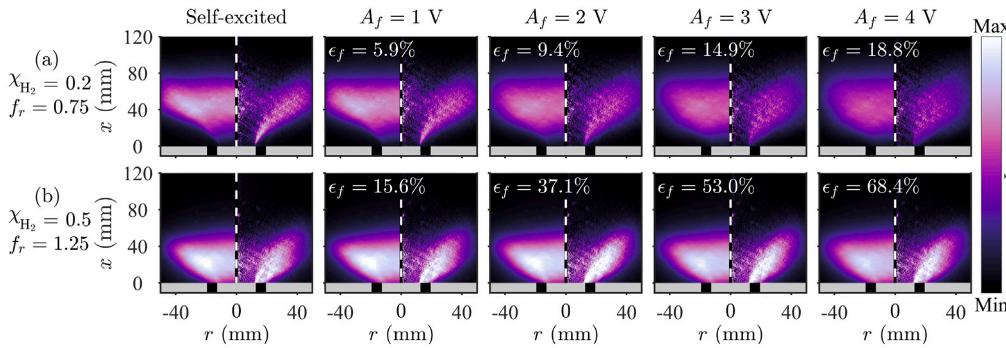

Fig. 8. The time-averaged OH* chemiluminescence intensity of the flame for (a) Case A (oscillation amplification) and (b) Case D (oscillation suppression), averaged over 100 forcing cycles. Each panel illustrates two visualizations: the average intensity distribution (left) and the Abel deconvoluted flame (right) at five different forcing amplitudes $A_f = 0$, 1, 2, 3, and 4 V (the corresponding ϵ_f are also annotated). Each panel is split by a white central dashed line for clear comparison. (For interpretation of the references to color in this figure legend, the reader is referred to the web version of this article.)

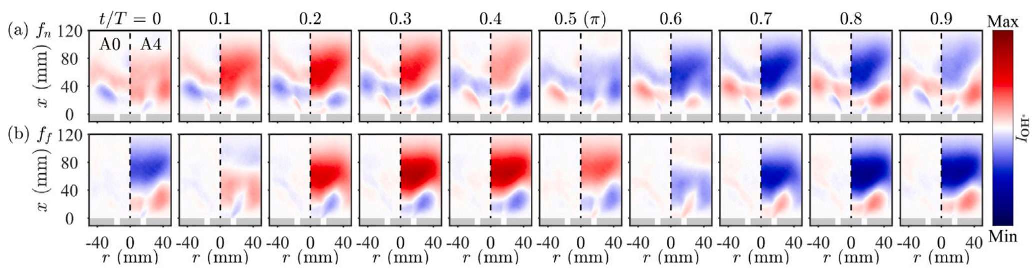

Fig. 9. The phase-averaged OH* chemiluminescence intensity of the flame over one cycle for (a) the f_n mode and (b) the f_f mode. Each mode is extracted from a sequence of flame images using a band-pass filter centered at the corresponding frequency, with a bandwidth of $\Delta f = \pm 5$ Hz, and subsequently averaged over 20 cycles. Each panel presents two visualizations: the average intensity distribution without acoustic forcing (i.e., unforced self-excited state, labeled A0, left) and with acoustic forcing (labeled A4, right, where $A_f = 4$ V, corresponding to $\epsilon_f = 18.8\%$). A black dashed line at the center of each panel separates the two visualizations for clearer comparison. (For interpretation of the references to color in this figure legend, the reader is referred to the web version of this article.)

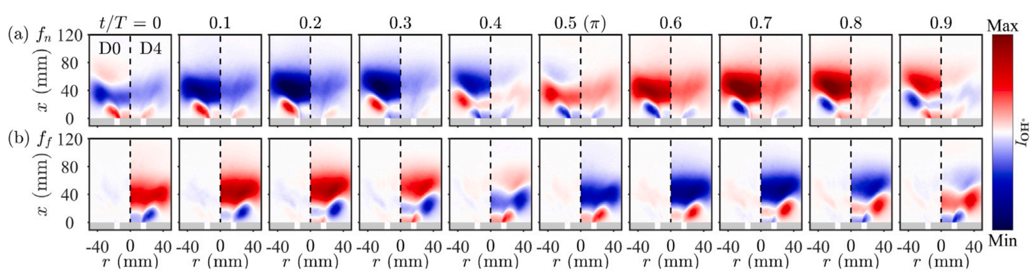

Fig. 10. The same as for Fig. 9 but for Case D, with $f_r = 1.25$ and $\epsilon_f = 68.4\%$ ($A_f = 4$ V). (For interpretation of the references to color in this figure legend, the reader is referred to the web version of this article.)

there is no external acoustic forcing, the OH* intensity of the flame at f_f remains negligible in both cases (Fig. 9b, left, and Fig. 10b, left).

We next examine the effect of acoustic forcing on the flame's mode shapes. Comparing the flame's mode shapes in Case A under unforced self-excited conditions (Fig. 9a, left) and with acoustic forcing at f_n (Fig. 9a, right) reveals a strong similarity in shape along the central black dashed line. However, due to the significant amplification of thermoacoustic oscillations in Case A (Fig. 11a), the OH* intensity of the flame subjected to acoustic forcing (A4) is substantially higher than that of the self-excited case (A0), indicating a strong flame response at f_f for this V-shaped flame. However, the coupling between p'_f and q'_f remains weak, resulting in negligible mode strength at f_f (see p'_f in Fig. 11a), as further corroborated by the absence of a distinct peak at f_f in Fig. 4c. In contrast, Case D exhibits a markedly different response to acoustic forcing. Comparing the mode shapes of the self-excited flame (Fig. 10a, left) and the acoustically forced flame at f_n (Fig. 10a, right), the flame retains its symmetric shape along the central axis; however, its OH* intensity is significantly lower under acoustic forcing. This reduction indicates a substantial weakening of the HRR fluctuations (i.e., q'_n), resulting in weaker coupling between q'_n and p'_n, thereby weakening the mode strength at f_n (see p'_n in Fig. 11b). At f_f, although the OH* intensity increases considerably under acoustic forcing (Fig. 10b, right), the corresponding increase in mode strength at f_f remains limited (see p'_f in Fig. 11b). As a result, the coupling between q'_f and p'_f does not significantly amplify oscillations. Consequently, the overall effect of acoustic forcing in Case D is the suppression of thermoacoustic oscillations, as evidenced by the reduced oscillation amplitude shown in Fig. 7a.

To summarize, our main findings in this section are as follows: (I) Oscillation suppression via open-loop acoustic forcing is primarily achieved by decoupling the flame dynamics from the acoustic field, as evidenced by the flattened distribution of $\Delta\psi_{\tilde{p}'-\tilde{q}'}$. From an energy perspective, when $\chi_{H_2} \geqslant 0.4$, the f_n mode is significantly weakened by the forcing and the additional acoustic energy input from the forcing remains limited, resulting in an overall reduction in total energy. This oscillation suppression mechanism shares a similar physical

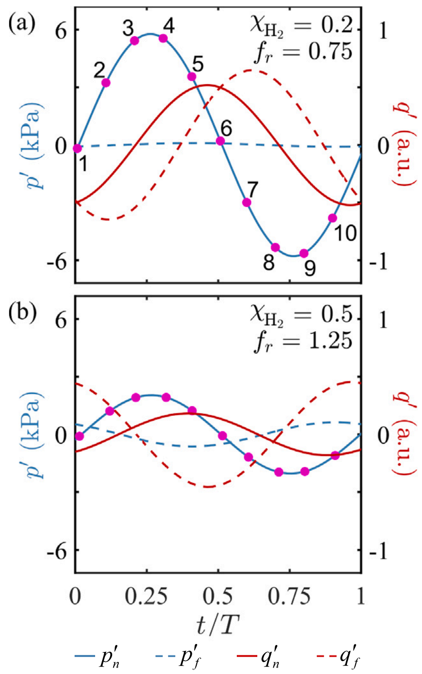

Fig. 11. The phase-averaged p' and q' components, band-pass filtered at f_n (subscript n) and f_f (subscript f) over one cycle, for (a) Case A and (b) Case D with acoustic forcing (A_f = 4 V), respectively. The magenta dots with labels on the p'_n curve correspond to the phases shown in Fig. 9 and Fig. 10. (For interpretation of the references to color in this figure legend, the reader is referred to the web version of this article.)

principle with those developed for conventional hydrocarbon-fueled combustors [37,42,62,63,66] and other thermoacoustic systems [67] employing open-loop acoustic forcing; (II) Oscillation amplification occurs when the coupling between the flame and acoustics fails to be disrupted. In this case, the f_n mode is further amplified by the applied forcing; and (III) Maximum oscillation suppression does not coincide with forced synchronization. The continued presence of the f_n mode is likely attributed to noise-induced resonance, where turbulence-generated noise in the flow continuously excites the system, preventing full suppression of the oscillations.

4. Conclusion

In this study, we experimentally investigate the effectiveness of open-loop acoustic forcing for active control of self-excited periodic thermoacoustic oscillations in a lean-premixed, H_2-enriched turbulent combustor. We have examined in a wide range of operating conditions, including variations in hydrogen volume fraction (χ_{H_2}), forcing frequency (f_f), and forcing amplitude (ϵ_f). We now proceed to address the research questions raised in Section 1.3:

1. Previous studies have demonstrated that open-loop acoustic forcing effectively weakens thermoacoustic oscillations in conventional hydrocarbon-fueled combustors at the off-resonant frequency and with sufficient forcing amplitudes. Is this control strategy still effective in mitigating thermoacoustic oscillations in a H_2-enriched turbulent combustor? What common characteristics does this H_2-enriched combustor share with previous conventional hydrocarbon-fueled combustors in terms of weakening thermoacoustic oscillations?
   For two research questions above: (I) Open-loop acoustic forcing, despite its simplicity in configuration, has proven to be still effective in suppressing thermoacoustic oscillations in our H_2-enriched turbulent combustor. The suppression effect becomes more pronounced with an increase in χ_{H_2}. Notably, this control approach is straightforward and energy-efficient, requiring the electrical power, which is equivalent to less than 1% of the combustor's thermal power, to achieve up to a 90% reduction in the amplitude of self-excited pressure oscillations; and (II) Similar to the oscillation suppression observed in conventional hydrocarbon-fueled combustors [37,42,62,63,66], the underlying characteristics of this suppression are based on a similar physical principle: disrupting the coupling between the flame dynamics and the acoustic field originally established at f_n. This disruption effectively attenuates the strength of the f_n mode. This study highlights the versatility of open-loop acoustic forcing as a robust strategy for mitigating oscillations in turbulent combustors with various fuel compositions.
2. If open-loop acoustic forcing is effective in suppressing thermoacoustic instabilities, how does its performance vary with different H_2 volume fractions in the fuel mixture? What are the optimal control strategies for open-loop acoustic forcing? What are the underlying physical mechanisms driving this control strategy?
   As χ_{H_2} increases, the effectiveness of active control of thermoacoustic oscillations via open-loop acoustic forcing is enhanced. The optimal control strategy involves applying large frequency detuning acoustic forcing ($f_r > 1$) for $\chi_{H_2} \geqslant 0.4$. However, this strategy should be used cautiously for $\chi_{H_2} \leqslant 0.3$ to avoid unwanted oscillation amplification. The underlying physical mechanism can be explained as follows: when the combustor is subjected to acoustic forcing at a non-resonant frequency f_f, the flame is then compelled to oscillate at that frequency where an effective energy feedback loop between p' and q' cannot be established. As a result, there is no significant accumulation of acoustic energy at f_f, and the originally established energy feedback loop at f_n is now disrupted because the flame dynamics are strongly dominated by the external forcing. Consequently, the general driving mechanism—described by the Rayleigh criterion—is weakened at f_n, leading to the decoupling between the flame dynamics and the acoustic field at f_n, and ultimately resulting in a reduction in the global oscillation amplitude.

The practical implications of this study are twofold: (I) We have demonstrated, for the first time, the effectiveness of open-loop acoustic forcing in mitigating self-excited periodic thermoacoustic oscillations in a H_2-enriched combustor. The underlying suppression mechanism in this decarbonized combustor resembles that observed in conventional hydrocarbon-fueled systems. This suggests that open-loop acoustic forcing, known for its simple configuration and robust control law design, could serve as a versatile strategy that may be adapted to existing conventional hydrocarbon-fueled facilities, potentially accelerating their decarbonization efforts; and (II) We have also shown that the suppression of thermoacoustic oscillations is significantly intensified at higher hydrogen volume fractions in the fuel mixture. This characteristic could be leveraged in future H_2-enriched combustion systems to actively force the flow or flame to oscillate at specific, designed frequencies, thereby avoiding more damaging frequencies that might resonate with system components. Additionally, it could complement passive control strategies, such as perforated plates or Helmholtz resonators, which are effective at other operational frequencies. Lastly, further work should be conducted to explore the effectiveness and universality of this open-loop oscillation suppression strategy across various thermoacoustic modes, including high-frequency modes observed in similar H_2-enriched combustors in our previous studies [10,68,69].

CRediT authorship contribution statement

Yu Liao: Writing – original draft, Formal analysis, Data curation. **Yongseok Choi:** Writing – review & editing, Data curation. **Peijin Liu:** Writing – review & editing. **Kyu Tae Kim:** Writing – review & editing, Funding acquisition. **Yu Guan:** Writing – review & editing, Methodology, Funding acquisition, Conceptualization.

Declaration of competing interest

The authors declare that they have no known competing financial interests or personal relationships that could have appeared to influence the work reported in this paper.

Acknowledgments

YL and YG were funded by the National Natural Science Foundation of China (Grant No. 52306166). YC and KTK were supported by the Korea Institute of Energy Technology Evaluation and Planning (KETEP) and the Ministry of Trade, Industry & Energy (MOTIE) of the Republic of Korea (Project No. 20214000000310, Human Resources Program in Energy Technology).

References

[1] P. Chiesa, G. Lozza, L. Mazzocchi, Using hydrogen as gas turbine fuel, J. Eng. Gas Turbines Power 127 (1) (2005) 73–80.
[2] D. Noble, D. Wu, B. Emerson, S. Sheppard, T. Lieuwen, L. Angello, Assessment of current capabilities and near-term availability of hydrogen-fired gas turbines considering a low-carbon future, J. Eng. Gas Turbines Power 143 (4) (2021) 041002.
[3] J. Beita, M. Talibi, S. Sadasivuni, R. Balachandran, Thermoacoustic instability considerations for high hydrogen combustion in lean premixed gas turbine combustors: a review, Hydrogen 2 (1) (2021) 33–57.
[4] T. Lieuwen, V. Yang, Combustion instabilities in gas turbine engines: operational experience, fundamental mechanisms, and modeling, AIAA, 2005.
[5] A. Morgans, D. Yang, Thermoacoustic instability in combustors, Annu. Rev. Fluid Mech. 57 (2024).
[6] M. Janus, G. Richards, M. Yip, E. Robey, Effects of ambient conditions and fuel composition on combustion stability, vol. 78699, ASME, 1997.
[7] S. Shanbhogue, Y. Sanusi, S. Taamallah, M. Habib, E. Mokheimer, A. Ghoniem, Flame macrostructures, combustion instability and extinction strain scaling in swirl-stabilized premixed CH_4/H_2 combustion, Combust. Flame 163 (2016) 494–507.
[8] J. Aguilar, E. Æsøy, J. Dawson, The influence of hydrogen on the stability of a perfectly premixed combustor, Combust. Flame 245 (2022) 112323.
[9] E. Æsøy, J. Aguilar, S. Wiseman, M. Bothien, N. Worth, J. Dawson, Scaling and prediction of transfer functions in lean premixed H_2/CH_4-flames, Combust. Flame 215 (2020) 269–282.
[10] T. Lee, K.T. Kim, High-frequency transverse combustion instabilities of lean-premixed multislit hydrogen-air flames, Combust. Flame 238 (2022) 111899.
[11] T. Lee, K.T. Kim, Combustion dynamics of lean fully-premixed hydrogen-air flames in a mesoscale multinozzle array, Combust. Flame 218 (2020) 234–246.
[12] K. Moon, Y. Choi, K.T. Kim, Experimental investigation of lean-premixed hydrogen combustion instabilities in a can-annular combustion system, Combust. Flame 235 (2022) 111697.
[13] K. Moon, H. Jegal, C. Yoon, K.T. Kim, Cross-talk-interaction-induced combustion instabilities in a can-annular lean-premixed combustor configuration, Combust. Flame 220 (2020) 178–188.
[14] G. Zhang, X. Wang, L. Li, X. Sun, Effects of perforated liners on controlling combustion instabilities in annular combustors, AIAA J. 58 (7) (2020) 3100–3114.
[15] L. Xu, J. Zheng, G. Wang, Z. Feng, X. Tian, L. Li, F. Qi, Investigation on the intrinsic thermoacoustic instability of a lean-premixed swirl combustor with an acoustic liner, Proc. Combust. Inst. 38 (4) (2021) 6095–6103.
[16] Z. Zhang, D. Zhao, N. Han, S. Wang, J. Li, Control of combustion instability with a tunable Helmholtz resonator, Aerosp. Sci. Technol. 41 (2015) 55–62.
[17] A. Gharehghani, K. Ghasemi, M. Siavashi, S. Mehranfar, Applications of porous materials in combustion systems: A comprehensive and state-of-the-art review, Fuel 304 (2021) 121411.
[18] R. Steele, L. Cowell, S. Cannon, C. Smith, Passive control of combustion instability in lean premixed combustors, J. Eng. Gas Turbines Power 122 (3) (2000) 412–419.
[19] Y. Guan, L. Li, H. Jegal, K.T. Kim, Effect of flame response asymmetries on the modal patterns and collective states of a can-annular lean-premixed combustion system, Proc. Combust. Inst. 39 (4) (2023) 4731–4739.
[20] T. Scarinci, C. Freeman, I. Day, Passive control of combustion instability in a low emissions aeroderivative gas turbine, in: ASME Turbo Expo, vol. 41669, 2004, pp. 487–499.
[21] J. Schluter, Static control of combustion oscillations by coaxial flows: a large-eddy-simulations investigation, J. Propul. Power 20 (3) (2004) 460–467.
[22] K. Moon, Y. Guan, L. Li, K.T. Kim, Mutual synchronization of two flame-driven thermoacoustic oscillators: Dissipative and time-delayed coupling effects, Chaos 30 (2) (2020).
[23] Y. Guan, Y. Choi, P. Liu, K.T. Kim, Mutual synchronization and flame dynamics in an axially fuel-staged lean-premixed combustion system, Proc. Combust. Inst. 40 (1–4) (2024) 105197.
[24] A. Dowling, A. Morgans, Feedback control of combustion oscillations, Annu. Rev. Fluid Mech. 37 (1) (2005) 151–182.
[25] K. McManus, T. Poinsot, S. Candel, A review of active control of combustion instabilities, Prog. Energy Combust. Sci. 19 (1) (1993) 1–29.
[26] S. Candel, Combustion dynamics and control: progress and challenges, Proc. Combust. Inst. 29 (1) (2002) 1–28.
[27] D. Zhao, Z. Lu, H. Zhao, X. Li, B. Wang, P. Liu, A review of active control approaches in stabilizing combustion systems in aerospace industry, Prog. Aerosp. Sci. 97 (2018) 35–60.
[28] N. Docquier, S. Candel, Combustion control and sensors: a review, Prog. Energy Combust. Sci. 28 (2) (2002) 107–150.
[29] P. Langhorne, A. Dowling, N. Hooper, Practical active control system for combustion oscillations, J. Propul. Power 6 (3) (1990) 324–333.
[30] J. Hermann, S. Hoffmann, Implementation of active control in a full-scale gas-turbine combustor, Prog. Aerosp. Sci. 210 (2005) 611.
[31] S. Murugappan, E. Gutmark, S. Acharya, Application of extremum seeking controller for suppression of combustion instabilities in spray combustion, in: 38th Aerospace Sciences Meeting and Exhibit, 2000, p. 1025.
[32] C. Paschereit, E. Gutmark, W. Weisenstein, Excitation of thermoacoustic instabilities by interaction of acoustics and unstable swirling flow, AIAA J. 38 (6) (2000) 1025–1034.
[33] A. Morgans, S. Stow, Model-based control of combustion instabilities in annular combustors, Combust. Flame 150 (4) (2007) 380–399.
[34] D. Bernier, S. Ducruix, F. Lacas, S. Candel, N. Robart, T. Poinsot, Transfer function measurements in a model combustor: application to adaptive instability control, Combust. Sci. Technol. 175 (5) (2003) 993–1013.
[35] A. Banaszuk, K. Ariyur, M. Krstić, C. Jacobson, An adaptive algorithm for control of combustion instability, Automatica 40 (11) (2004) 1965–1972.
[36] S. Illingworth, A. Morgans, Adaptive feedback control of combustion instability in annular combustors, Combust. Sci. Technol. 182 (2) (2010) 143–164.
[37] Y. Guan, V. Gupta, K. Kashinath, L. Li, Open-loop control of periodic thermoacoustic oscillations: experiments and low-order modelling in a synchronization framework, Proc. Combust. Inst. 37 (4) (2019) 5315–5323.
[38] G. Richards, J. Thornton, E. Robey, L. Arellano, Open-loop active control of combustion dynamics on a gas turbine engine, J. Eng. Gas Turbines Power 129 (1) (2007) 38–48.
[39] T. Yi, E. Gutmark, Combustion instabilities and control of a multiswirl atmospheric combustor, J. Eng. Gas Turbines Power 129 (1) (2007) 31–37.
[40] B. Bellows, A. Hreiz, T. Lieuwen, Nonlinear interactions between forced and self-excited acoustic oscillations in premixed combustor, J. Propul. Power 24 (3) (2008) 628–631.
[41] B. Ćosić, B. Bobusch, J. Moeck, C. Paschereit, Open-loop control of combustion instabilities and the role of the flame response to two-frequency forcing, J. Eng. Gas Turbines Power 134 (6) (2012).
[42] S. Balusamy, L. Li, Z. Han, M. Juniper, S. Hochgreb, Nonlinear dynamics of a self-excited thermoacoustic system subjected to acoustic forcing, Proc. Combust. Inst. 35 (3) (2015) 3229–3236.
[43] F. Lückoff, K. Oberleithner, Excitation of the precessing vortex core by active flow control to suppress thermoacoustic instabilities in swirl flames, Int. J. Spray Combust. Dyn. 11 (2019) 1756827719856237.
[44] S. Mahesh, R. Gopakumar, B. Rahul, A. Dutta, S. Mondal, S. Chaudhuri, Instability control by actuating the swirler in a lean premixed combustor, J. Propul. Power 34 (3) (2018) 708–719.
[45] A. Alkhalifa, A. Alsalem, D. Del Cont-Bernard, D. Lacoste, Active control of thermoacoustic fluctuations by nanosecond repetitively pulsed glow discharges, Proc. Combust. Inst. 39 (4) (2023) 5429–5437.
[46] Q. Malé, S. Shcherbanev, M. Impagnatiello, N. Noiray, Stabilization of a thermoacoustically unstable sequential combustor using non-equilibrium plasma: Large eddy simulation and experiments, Proc. Combust. Inst. 40 (1–4) (2024) 105277.
[47] K. Moon, D. Bae, K.T. Kim, Modal dynamics of self-excited thermoacoustic instabilities in even and odd numbered networks of lean-premixed combustors, Combust. Flame 255 (2023) 112928.
[48] Y. Guan, K. Moon, K.T. Kim, L. Li, Synchronization and chimeras in a network of four ring-coupled thermoacoustic oscillators, J. Fluid Mech. 938 (2022) A5.

[49] D. Goodwin, R. Speth, H. Moffat, B. Weber, Cantera: An object-oriented software toolkit for chemical kinetics, thermodynamics, and transport processes, Zenodo, 2018.
[50] G. Smith, D. Golden, M. Frenklach, N. Moriarty, B. Eiteneer, M. Goldenberg, C. Bowman, R. Hanson, S. Song, W. Gardiner, V. Lissianski, Z. Qin, GRI-mech 3.0, 2024.
[51] Y. Guan, V. Gupta, M. Wan, L. Li, Forced synchronization of quasiperiodic oscillations in a thermoacoustic system, J. Fluid Mech. 879 (2019) 390–421.
[52] Y. Guan, B. Yin, Z. Yang, L. Li, Forced synchronization of self-excited chaotic thermoacoustic oscillations, J. Fluid Mech. 982 (2024) A9.
[53] R. Sujith, V. Unni, Dynamical systems and complex systems theory to study unsteady combustion, Proc. Combust. Inst. 38 (3) (2021) 3445–3462.
[54] F. Takens, Detecting strange attractors in turbulence, in: Dyn. Syst. Turbul., vol. 898, Springer, 1981, pp. 366–381.
[55] H. Kantz, T. Schreiber, Nonlinear time series analysis, Cambridge University Press, 2003.
[56] A. Fraser, H. Swinney, Independent coordinates for strange attractors from mutual information, Phys. Rev. A 33 (2) (1986) 1134.
[57] L. Cao, Practical method for determining the minimum embedding dimension of a scalar time series, Phys. D 110 (1–2) (1997) 43–50.
[58] K.T. Kim, J. Lee, H. Lee, B. Quay, D. Santavicca, Characterization of forced flame response of swirl-stabilized turbulent lean-premixed flames in a gas turbine combustor, J. Eng. Gas Turbines Power 132 (4) (2010) 041502.
[59] T. Guiberti, D. Durox, P. Scouflaire, T. Schuller, Impact of heat loss and hydrogen enrichment on the shape of confined swirling flames, Proc. Combust. Inst. 35 (2) (2015) 1385–1392.
[60] J. Lachaux, E. Rodriguez, J. Martinerie, F. Varela, Measuring phase synchrony in brain signals, Hum. Brain Mapp. 8 (4) (1999) 194–208.
[61] A. Pikovsky, M. Rosenblum, J. Kurths, Synchronization: A universal concept in nonlinear sciences, Cambridge University Press, 2001.
[62] Y. Guan, W. He, M. Murugesan, Q. Li, P. Liu, L. Li, Control of self-excited thermoacoustic oscillations using transient forcing, hysteresis and mode switching, Combust. Flame 202 (2019) 262–275.
[63] P. Wang, Y. Tian, L. Yang, S. Luo, J. Li, T. Liu, Open-loop control of thermoacoustic instabilities by the external acoustic forcing at different frequencies, Proc. Combust. Inst. 40 (1–4) (2024) 105540.
[64] E. Æsøy, T. Indlekofer, F. Gant, A. Cuquel, M. Bothien, J. Dawson, The effect of hydrogen enrichment, flame-flame interaction, confinement, and asymmetry on the acoustic response of a model can combustor, Combust. Flame 242 (2022) 112176.
[65] A. Roy, S. Mondal, S. Pawar, R. Sujith, On the mechanism of open-loop control of thermoacoustic instability in a laminar premixed combustor, J. Fluid Mech. 884 (2020) A2.
[66] B. Yin, Z. Yang, Y. Guan, S. Redonnet, V. Gupta, L. Li, Genetic programing control of self-excited thermoacoustic oscillations, Phys. Fluids 36 (6) (2024).
[67] S. Mondal, S. Pawar, R. Sujith, Forced synchronization and asynchronous quenching of periodic oscillations in a thermoacoustic system, J. Fluid Mech. 864 (2019) 73–96.
[68] H. Kang, K.T. Kim, Combustion dynamics of multi-element lean-premixed hydrogen-air flame ensemble, Combust. Flame 233 (2021) 111585.
[69] Y. Choi, K.T. Kim, Strong flame interaction-induced collective dynamics of multi-element lean-premixed hydrogen flames, Int. J. Hydrog. Energy 48 (5) (2023) 2030–2043.